A Nonlinear Optimization Technique for Ground-Based Atmospheric Emission Tomography

Joshua Semeter and Michael Mendillo

***Abstract*—Solar-terrestrial interactions produce a rich variety of optical emissions in the Earth's upper atmosphere (100–1000 km). While ground based brightness measurements (i.e., column integrated photon density) provide an important diagnostic of these processes, the more interesting physics is in the associated volume emission rate distribution (i.e., photon production/cm^3 s versus altitude). This work examines a new technique for remote sensing of the Earths' radiative environment. Brightness measurements from a network of ground-based imaging systems are used to define a limited angle emission tomography problem, from which two-dimensional (2-D) (latitude versus altitude) volume emission rate profiles are reconstructed.**

The incomplete angular coverage imposed by this viewing geometry leads to an ill-posed and ill-conditioned inverse problem. The problem is regularized by initially constraining the vertical profiles to be Chapman functions. Such a parameterization captures the mean features of a large class of emission structures. A weighted Euclidean distance between the measured and estimated data is then minimized, subject to side constraints that define the feasibility region for the Chapman parameters. The side constraints are implemented as barrier functions, resulting in an unconstrained nonlinear optimization problem. Minimization is performed using the Broyden–Fletcher–Goldfarb–Shanno variant of the Davidon–Fletcher–Powell (DFP) method. The resulting volume emission rate elements are then used as an initial guess to a multiplicative algebraic reconstruction (MART) algorithm. In addition to regularizing the problem, this technique exposes important geometrical limitations to this class of inverse problem.

***Index Terms*— Airglow, aurora, ionosphere, nonlinear optimization, tomography.**

I. Introduction

THE chemical and dynamical processes of the Earth's upper atmosphere produce optical emissions at a variety of wavelengths and a wide range of intensities [1]–[3]. Examples include the aurora at high latitudes, a ubiquitous chemically induced neutral airglow, and thermally excited Stable Auroral Red (SAR) Arcs. The integrated column brightness of these features can vary from 10 to $>10^4$ Rayleighs (1 Rayleigh $= 10^6$ photons/cm^2 s). Airglow has also been created "artificially" through chemicals released from space vehicles [4]–[6]. Observations of atmospheric emissions by standard spectroscopic and photometric means have led to many fundamental advances in aeronomy. New techniques and instrumentation continue to make optical aeronomy a vital method for studying the solar-terrestrial environment.

Ground-based imaging of the atmosphere's optical environment provides two-dimensional (2-D) projections (i.e., surface brightness maps) of three-dimensional (3-D) structures (i.e., volume emission rate distributions). It is in the latter *intrinsic* parameter that the interesting fundamental atmospheric processes occur. For the case of plasma species in the ionosphere, intrinsic parameters such as electron densities and temperatures can be directly sensed using Incoherent Scatter (IS) and High Frequency backscatter (HF) radars. LIDAR's have allowed the direct access of volume emission height profiles through laser fluorescence of atmospheric species [7]. However, their applicability has been limited to the mesosphere (80–110 km) [8], [9]. As of yet, a technique has not been developed to reconstruct the volume emission rate profiles associated with passive ground-based optical measurements.

Tomography has recently emerged as an important technique for exploring the spatial dependence of upper atmospheric features. Satellite-based tomography using photometric observations was first attempted during NASA's Atmospheric Explorer program [10], [11]. Large scale tomographic imaging of the Earths radiative environment are the goals of current rocket [12] and satellite programs [13]. Ionospheric radio tomography using measurements of total electron content (TEC) between a transmitting satellite and a network of ground receivers has received much attention recently [14]–[16]. In this case, the reconstructed profile is of electron density versus altitude $N_e(h)$. The related *ground-based optical tomography* problem has the advantage of requiring no satellite involvement and, as such, is the subject of this work. In this technique, one-dimensional (1-D) images (brightness versus elevation angle) of an optically thin emission are recorded from a network of imaging spectrographs. These measurements are used to define a system of integral equations from which 2-D (latitude versus altitude) volume emission profiles are estimated. The problem is illustrated schematically in Fig. 1. Three observing stations are shown, and both the observations and the emitting region have been discretized.

The problem can be thought of as a limited-angle, fan-beam tomography problem [17]. The observations are limited to the surface of a sphere (the Earth). In contrast to medical tomography, the object under observation is outside this sphere (as shown schematically in Fig. 2). With such geometry, even modest binning in the altitude direction introduces more degrees of freedom than are supported by the data (leading to a

Manuscript received July 21, 1996; revised February 28, 1997. This work was supported in part by NSF Grants ATM-9402269 and ATM-9203198 from Boston University.

The authors are with the Department of Electrical and Computer Engineering and the Center for Space Physics, Boston University, Boston, MA 02215 USA.

Publisher Item Identifier S 0196-2892(97)05510-1.

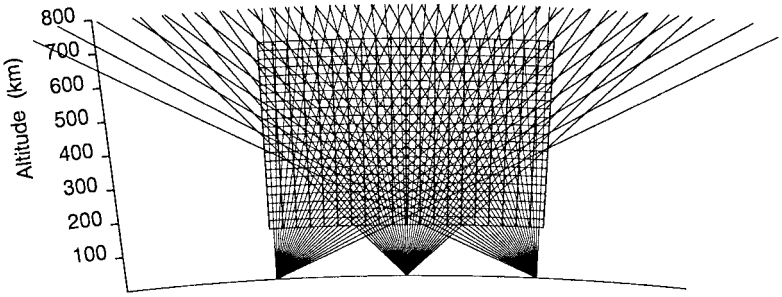

Fig. 1. Schematic representation of the GAET problem. In this work, the observations and the emitting region are discretized *a priori*.

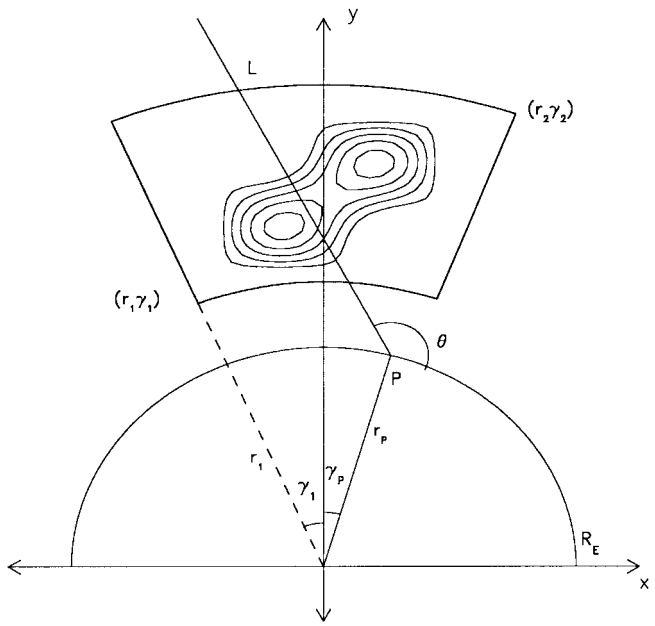

Fig. 2. The viewing geometry for GAET can be compared to a fan-beam tomography problem. A given observation is defined by θ and γ_p (assuming r_p is constant).

so-called *ill posed* problem). To obtain a meaningful solution to this linear inverse problem (i.e., a plausible solution that deviates significantly from an initial guess), some *a priori* assumptions must be made. In ionospheric radio beacon tomography, a typical approach is to constrain the solution to be a linear combination of a set of basis ionospheres. Oftentimes, however, these algorithms yield solutions that retain kernel features of the initial guess. Typically, these algorithms favor percentage adjustments to the electron densities, while leaving the altitude of the peak electron density and the characteristic width of the electron density profile unchanged.

In this work, ground-based atmospheric emission tomography (GAET) is approached as a nonlinear optimization problem. At a given horizontal position, the vertical profile is initially constrained to be a *Chapman* function (a nonlinear function described by three parameters). Such a parameterization introduces *a priori* the characteristics of emission versus altitude we are likely to be concerned with, namely, the peak emission rate, the altitude where the peak emission occurs, and the width of the emission layer (related to the scale heights of the source particles). The validity of this approach rests with rocket-borne photometer measurements [18] and theory [1] which show that emission profiles tend to be unimodal, with a larger scale height on the topside. The final solution is allowed to deviate from the Chapman profiles, but these deviations will be in the neighborhood of the parameterized solution. The algorithm allows robust reconstruction of a large class of atmospheric emission features with reasonable computation time.

This technique also provides important insight into the limitations imposed by the GAET viewing geometry. The direct inverse problem is poorly conditioned and the solution will vary greatly depending on the starting point of the inversion. Fortunately, most solutions are meaningless within the context of what is known physically about emission profiles. The Chapman regularization mitigates, but does not completely eliminate, this problem. The technique and results presented here are relevant to the ionospheric radio beacon tomography problem as well, and thus merit some in-depth discussion and simulation.

II. Preliminaries

The calibrated quantity for observations of the brightness of widely distributed sources (such as those originating in the Earth's upper atmosphere) is the *Rayleigh*. It is appropriate to speak of the brightness in Rayleighs (R) of an emitting object when its scale size is greater than the resolution element of the measuring device [1]. This is the case with CCD based imaging devices currently used in atmospheric science [19]. A typical field of view for an individual pixel is a half a degree, corresponding to a horizontal distance of 5 km at ionospheric altitudes ($\sim$300 km).

Let $v(\mathbf{r})$ represent the volume emission rate of an isotropic source at position $\mathbf{r}$ in photons/cm^3 s.[1] For an optically thin emission, the brightness at a position P is defined as

$$R_P = 10^{-6} \int_0^\infty v(\mathbf{l}) \cdot d\mathbf{l} \quad [10^6 \text{ photons/cm}^2/\text{s}] \qquad (1)$$

where $d\mathbf{l}$ defines a particular line of sight from point P, and R_P is the column integrated brightness due to $v(\mathbf{l})$.

Fig. 2 illustrates schematically the unique geometry associated with atmospheric emission tomography (not to scale). The emitting region is shown as contours within a confined region of latitude and altitude. With respect to the Earth centered geometry shown in Fig. 2, a line L through the atmosphere at

[1]The subsequent development assumes $v(\mathbf{r})$ to be isotropic. For further discussion, see [1].

angle θ and from a point $P = (r_p, \gamma_p)$ is described by

$$y = \tan(\theta - \gamma_p)\, x + r_p[\cos\gamma_p - \tan(\theta - \gamma_p)\, \sin\gamma_p] \quad (2)$$

where $r_p = R_e + [\text{site altitude}]$, γ_p is the site latitude, and θ is the observation angle. In general, deviations of r_p from R_E are negligible compared to the resolution of the tomographic reconstruction. However, significant errors will result if a "flat Earth" assumption is made.

In terms of the parameters of Fig. 2, (1) can be rewritten

$$\begin{aligned} R_{r_p,\gamma_p}(\theta) = 10^{-6} \int_0^\infty \int_0^\infty v(x, y) \\ \times \delta\{y - \tan(\theta - \gamma_p)x - r_p \\ \times [\cos\gamma_p - \tan(\theta - \gamma_p)\, \sin\gamma_p]\}\, dx\, dy \end{aligned} \quad (3)$$

where δ is the dirac delta function. In a practical problem, the emission is assumed to be confined to latitude range (γ_1, γ_2) and altitude range (r_1, r_2) as indicated in Fig. 2. Under these assumptions, and converting to a more convenient polar coordinate system, (3) becomes

$$\begin{aligned} R_{\gamma_p}(\theta) = 10^{-6} \int_{r_1}^{r_2} \int_{\gamma_1}^{\gamma_2} v(r, \gamma) \\ \times \delta\{R_E\cos\gamma_p - \tan(\theta - \gamma_p)R_E\sin\gamma_p \\ - R_E[\cos\gamma_p - \tan(\theta - \gamma_p)\, \sin\gamma_p]\}\, d\gamma\, dr. \end{aligned} \quad (4)$$

Equation (4) is a variant of the radon transform for *fan-beam* tomography. It maps $v(r, \gamma)$ into $R_{\gamma_p}(\theta)$. As in the related medical tomography problem, observations are confined to a "circle" (the Earth). In this case, however, the object sits *outside* the circle.

The inversion technique described here is in the class of finite series expansion techniques [17], as opposed to transform techniques. In this approach, the emitting region is discretized *a priori* into a set of volume emission rate pixels (hereafter called "voxels"). Discretizing the right side of (4), we may write

$$R_{\gamma_p}(\theta) = \sum_{i=0}^{I} \sum_{j=0}^{J} v_{ij} l_{ij}(\gamma_p, \theta) \quad (5)$$

where I is the number of latitudes, J is the number of altitudes, and $l_{ij}(\gamma_p, \theta)$ is the length of the line of sight defined by (γ_p, θ) in voxel v_{ij}. The l_{ij} are readily calculated given the geometry illustrated in Fig. 2 and described by (4). If the l_{ij} are in units of 10^6 cm $= 10$ km and the v_{ij} are in units of photons/cm^3 s, then $R_{\gamma_p}(\theta)$ will be in Rayleighs. In other words, the l_{ij} may be conveniently left in units of km when considering (5). The resulting v_{ij} need only be multiplied by a factor of ten to obtain the standard volume–emission–rate unit of photons/cm^3 s.

When the set of observations is also discretized, (5) may be written

$$R_k = \sum_{j=0}^{J} \sum_{i=0}^{I} v_{ij} l_{ijk}. \quad (6)$$

In the absence of noise or atmospheric effects, R_k is the observed brightness at position and look direction $(\gamma_P, \theta)_k$. The angle γ_P represent the location of an instruments on some great circle. In practice, there are two to four instrument locations, all lying on the same great circle, with roughly 200 look directions (θ) at each site. Observations made from a real digital instrument are subject to four significant sources of uncertainty: 1) the instrument point spread function, 2) photon counting statistics, 3) photon absorption, and 4) tropospheric scattering. The point spread function for the instrumentation used in this study (described in detail in [19]) is less than three pixels. This degrades the spatial resolution in the zenith to about 10 km at 300 km altitude. The point spread function is not a limiting factor in GAET. For very faint emissions, it is important to consider Poisson statistics associated with the optical device. For the rather large fluxes ($>50R$) associated with the emissions considered here, the photon counting statistic becomes Gaussian. Photon loss due to absorption has been well studied for the entire spectrum [20] and follows a $\sec\chi$ dependence, where χ is the zenith angle. Absorption can be included as an *a priori* adjustment to the observations. The more difficult uncertainty is in tropospheric effects. Mie scattering and albedo effects in the lower atmosphere significantly affect the photon flux at the instrument. These effects are less well understood quantitatively, but can be assumed to impose a higher uncertainty in the data at larger zenith angles.

In terms of (6), tropospheric scattering and photon counting statistics can be considered additive noise sources. Photon absorption is a constant multiplicative adjustment. The adjusted brightness measurements, d_k, are now related to the voxel values as

$$d_k = a_k \sum_{j=0}^{J} \sum_{i=0}^{I} v_{ij} l_{ijk} + n_k \quad (7)$$

or as a matrix equation

$$\mathbf{d} = \mathbf{a}(\mathbf{L} \cdot \mathbf{v}) + \mathbf{n} \quad (8)$$

where $l_{ijk} = 10 \times$ [length of measurement d_k in voxel v_{ij} in km] (as discussed previously), n_k is a random variable representing the uncertainty of measurement d_k, and a_k is the brightness adjustment due to the atmospheric absorption model. Each of the K elements of vector $\mathbf{d}$ is an *apparent* brightness in Rayleighs (as described in Appendix II of [1]).

III. Regularizing the GAET Inverse Problem

The linear system described by (8) is both sparse and ill-conditioned. Although there are generally many more projections than model elements (i.e., $K > I \times J$), the linear system is nonetheless underdetermined. This can be seen intuitively by examining Fig. 1. There may be as many as 200 lines-of-site at each of the three projection angles shown. However, adjacent rays are nearly parallel, and hence the columns of $\mathbf{L}$ are nearly linearly dependent. Although $\mathbf{L}$ is not singular, it is nearly singular.

In the case of ideal noiseless data (i.e., $\mathbf{a} = 1$, $\mathbf{n} = 0$), we may nonetheless obtain a solution by direct inversion of $\mathbf{L}$. It is quickly found that although this solution minimizes the residual two-norm (i.e., $\min \|\mathbf{d} - \mathbf{L} \cdot \mathbf{v}\|_2$), it will be highly oscillatory and contain large negative values for any reasonable

number of solution elements. The solution must, therefore, be regularized.

Most standard regularization techniques remove undesirable behavior by trading off minimization of the residual norm with minimization of some solution seminorm. The best known of these is Tikhonov regularization, which minimizes an objective of the form

$$\mathbf{v} = \text{argmin } \{||\mathbf{d} - \mathbf{L} \cdot \mathbf{v}||_2 - \alpha||\mathbf{\Lambda} \cdot (\mathbf{v} - \mathbf{v}^*)||_2\} \quad (9)$$

where Λ represents a linear operator and α controls the degree of regularization. The initial guess may be included as $\mathbf{v}^*$. These techniques also fail to produce acceptable solutions for GAET. Simply stated, the amount of regularization required to remove the undesirable solutions results in an unacceptably large residual norm. For anything but the very simplest fields, standard regularization techniques blur out all but the coarsest features when applied to GAET.

In light of such extreme ill-conditioning, we now replace the unconstrained inverse problem with an inverse problem that imposes some *a priori* knowledge about the solution. Rather than introduce a constraint on the solution norm, we return to the problem of minimizing the residual norm or

$$\min ||\mathbf{d} - \mathbf{L} \cdot \mathbf{v}||_2. \quad (10)$$

However, we now constrain $\mathbf{v}$ to have certain average features we expect to observe in atmospheric emitting layers.

A. The Chapman Function

From Fig. 1, it can be inferred that the solution to the GAET problem has greater support in the horizontal dimension than the vertical dimension. One way to mitigate this problem is to impose a parameterization in the vertical direction. A judicious choice of parameterizing function will reduce the dimensionality in the vertical while also capturing the expected shape of an emission layer. Theoretical studies of airglow and aurora have shown that the vertical emission profile at a point P should be unimodal. Moreover, emission profiles generally have a steeper gradient (i.e., smaller scale height) on the bottomside than on the topside [21]. An altitude profile fitting this model and described by three parameters is the Chapman function[2] [22]. Given three parameters: the maximum volume emission rate V^m [photons/cm^3 s], the altitude of the maximum volume emission rate Z^m [km], and a characteristic emission width H [km], the volume emission rate at any altitude z is given by

$$v^c(z) = V^m \exp[0.5(1 - z1 - \exp(-z1)] \quad (11)$$

where

$$z1 = \frac{z - Z^m}{H} \quad (12)$$

where v^c is used to indicate Chapman-constrained volume emission rates. Fig. 3 illustrates a Chapman function for two different values of H.

[2] Sydney Chapman, 1931. Equations (11) and (12) were developed to described electron density as a function of height in the "simple Chapman model" of ionospheric formation. We use this formalism as a convenient mathematical representation of optical emission profiles, a topic not actually treated in Chapman theory.

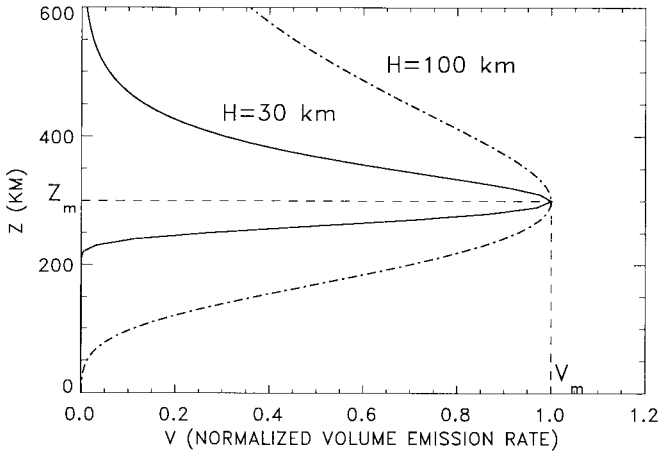

Fig. 3. The mean features of the vertical profile of an atmospheric emission may be described by a Chapman function. Three parameters are required: the peak emission rate, V^m, the height of this peak, Z^m, and the characteristic width, H. Two examples are shown here.

Other functions characterized by three such parameters may be considered as well. For example, a Gaussian function is described by a peak magnitude, the position of the peak and the standard deviation. Any such function could be used to regularize this problem. The choice of Chapman functions reflects prior knowledge that atmospheric emitting layers are not, in general, symmetric, but have sharper gradients below the peak in comparison to those above Z^m. However, it should be noted that in this context, the Chapman function is used as a convenient mathematical form for an emitting layer, and hence it is most accurate to refer to H as a "characteristic width" rather than the "scale height." Both the Gaussian function and the Chapman function have infinite support and are continuously differentiable. These features are desirable for optimization problems.

Given a set of $I \times 3$ Chapman parameters, the resulting voxel values are given by

$$v^c_{ij} = V^m_i \exp[0.5(1 - z1_{ij} - \exp(-z1_{ij})] \quad (13)$$

with

$$z1_{ij} = \frac{z_j - Z^m_i}{H_i}. \quad (14)$$

The unknowns are now reduced from $I \times J$ volume emission rates to $I \times 3$ Chapman parameters.

B. The Nonlinear Objective Function

The misfit to the data is represented by the weighted Euclidean norm (or two-norm) between the observed data $\mathbf{d}$ and the estimated data $\mathbf{d}^{est} = \mathbf{a}(\mathbf{L} \cdot \mathbf{v}^c)$.

$$E(\mathbf{V}^m, \mathbf{Z}^m, \mathbf{H}) = \left\| \frac{\mathbf{d} - \mathbf{a}(\mathbf{L} \cdot \mathbf{v}^c)}{\mathbf{w}} \right\|_2 \quad (15)$$

where $\mathbf{v}^c$ is the matrix of voxel values resulting from a Chapman parameterization and $\mathbf{w}$ is a vector of weights that characterizes the uncertainty associated with each measurement.

If $\mathbf{d}$ is assumed to be a random vector with Gaussian statistics, $\mathbf{w}$ is the vector of standard deviations, $\boldsymbol{\sigma}$. The σ_k

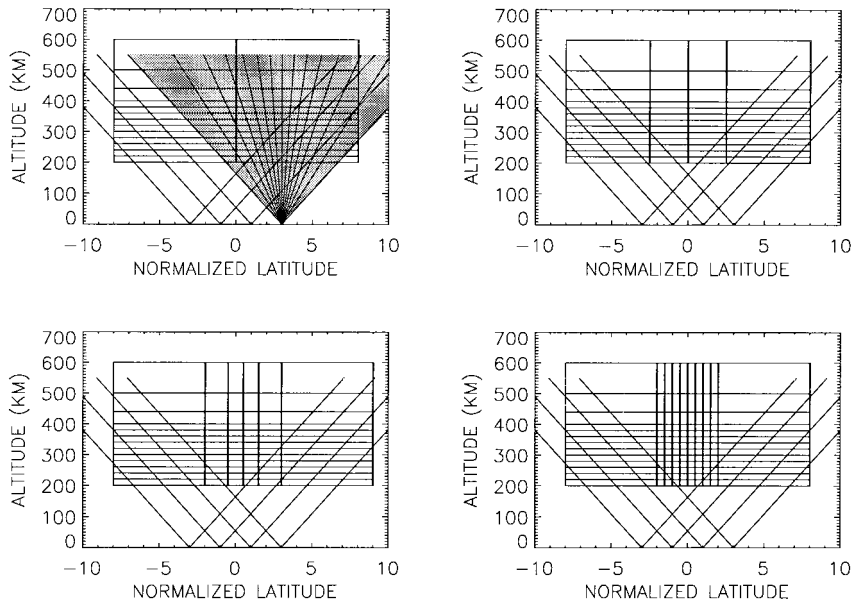

Fig. 4. To facilitate convergence, the solution is sought on a progressively finer *horizontal* gridding. The vertical gridding is constant, a suitable resolution being about 10 km. Shown are samples of a typical gridding scheme with outlines of the instruments' fields of view.

may be estimated experimentally, and for a given instrument, may be considered to be constant over the field of view.

However, the w_k are also used to account for uncertainties due to tropospheric effects. The uncertainty in absolute brightness is greater at larger zenith angles, χ. Therefore, at each iteration, we would like the solution to favor fitting the data at smaller χ (i.e., near the zenith). A reasonable choice for $\mathbf{w}$ is in fact $C\sec\chi$, with C a scaling constant. This is the same form as the photon absorption model. To include both atmospheric and instrumental uncertainties in the tomographic reconstruction then, $\mathbf{w}$ will have the form

$$\mathbf{w} = C\sigma\ \sec(\boldsymbol{\chi}) \tag{16}$$

where σ is now assumed to be constant. The scaling constant C is used to bound E, and is usually set to the length of $\mathbf{d}$. If no atmosphere is present (e.g., in satellite tomography), then this choice of C allows for a physical interpretation of E as the average residual divided by the standard deviation. The minimization of E would then proceed until $E \sim 1$. Further iteration would fit the noise.

C. Constraining the Feasibility Region

Equation (15) is nonlinear in $\mathbf{Z}^m$ and $\mathbf{H}$. As will be demonstrated, convergence will generally require additional side constraints to guide the solution away from known unwanted minima. We, therefore, define the feasibility region for $\mathbf{v}^c$ as

$$\text{constraints} \begin{cases} V^m & \geq & 0 \\ Z_h^m & > & Z_i^m > Z_l^m \\ H_h & > & H_i > H_l. \end{cases} \tag{17}$$

E is a linear function of V^m. Convexity over V^m is thus guaranteed, given that E is convex over Z^m and H. The choice of the constants Z_h^m, Z_l^m, H_h, and H_l are dictated by known general limits of occurrence; for example, sufficient

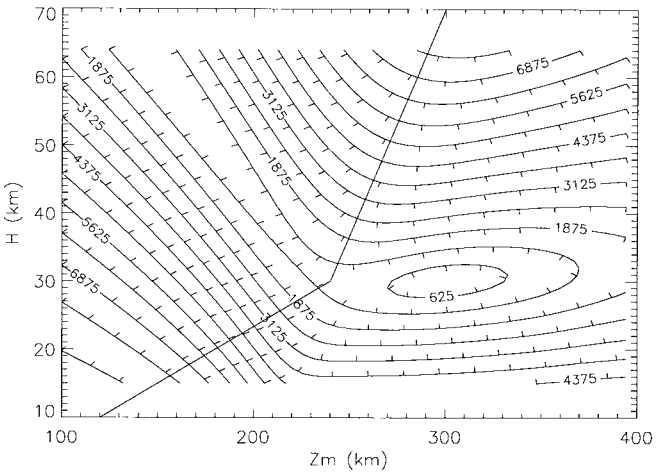

Fig. 5. A contour plot of E versus Z^m and H for the a simple uniform stratified emitting region ($V^m = 1, H = 30, Z^m = 300$). Although the global minimum is evident by inspection, if the initial guess is to the left of the partition line drawn E will converge to a point in the "valley" (i.e., a small Z^m and a large H).

constraints for a Stable Auroral Red Arc or ambient airglow are $Z_h^m = 700$ km, $Z_l^m = 100$ km, $H_h = 70$ km, and $H_l = 10$ km.

Within the feasible solution set, the best set of $I \times 3$ Chapman parameters will satisfy

$$\min\{E(\mathbf{V}^m, \mathbf{Z}^m, \mathbf{H}) |\ \text{constraints}\}. \tag{18}$$

A convenient method of imposing inequality constraints is with the use of *barrier* functions [23]. In this technique, the constrained optimization problem is converted to an unconstrained optimization as follows. First using the lower boundary as an example, rewrite the constraints as

$$g_1(\mathbf{V}^m) = \mathbf{V}^m > 0 \tag{19}$$

$$g_2(\mathbf{Z}^m) = \mathbf{Z}^m - Z_l^m > 0 \tag{20}$$

$$g_3(\mathbf{H}) = \mathbf{H} - H_l > 0. \tag{21}$$

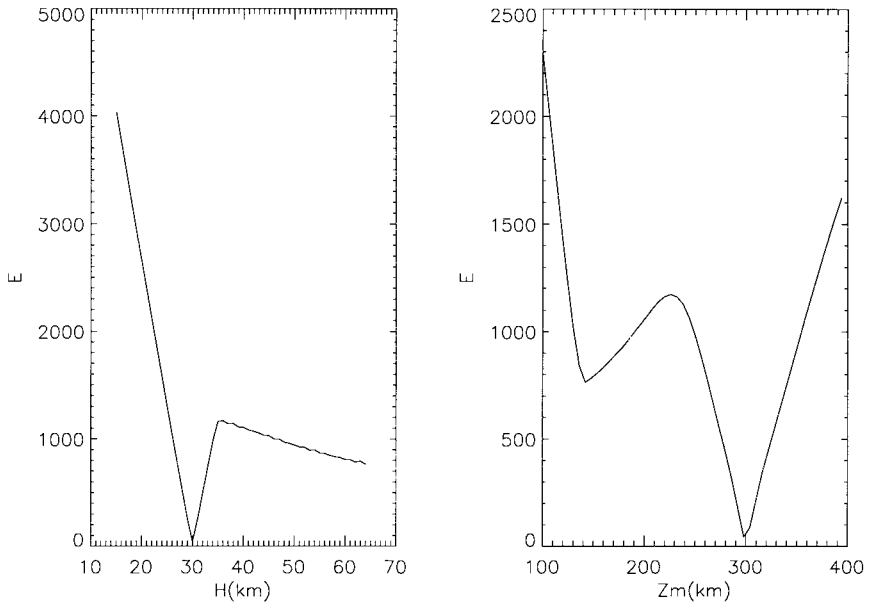

Fig. 6. A plot of E along the valley of Fig. 5. The true solution is at $H = 30$ and $Z^m = 300$, but other local minima are evident. Thus, even in such simple GAET problems, the solution depends on the initial guess and the robustness of the algorithm in avoiding local minima.

A standard barrier function of the form $-r \ln[-g(\mathbf{x})]$ is used here. The resulting unconstrained optimization problem then has the objective

$$E - \lambda_1 r \ln[g_1(\mathbf{V^m})] - \lambda_2 r \ln[g_2(\mathbf{Z}^m)] - \lambda_3 r \ln[g_3(\mathbf{H})] \tag{22}$$

where the λ_q are weighting functions chosen to normalize the relative magnitudes of the Chapman parameters. For the GAET problem, the convergence of (22) does not depend heavily on the values chosen for the λ_q. The parameter r scales the influence of the barrier functions. As the minimization proceeds, r should approach zero geometrically. Equation (22) then approaches the unconstrained minimization of (15). In the present algorithm, at each iteration we set $r_{\text{new}} = r_{\text{old}}/2$.

The advantage to using barrier functions is to give a smooth penalty to violations of the feasibility region. Moreover, we retain a continuously differentiable objective function. The explicit gradient information allows us to use a geometrically convergent variable-metric algorithm [24], described in the following section.

D. Minimization of E

Scientifically useful results can be obtained in GAET from a reasonably sized optimization problem. A typical experimental configuration will cover about 7° of latitude. A maximum useful horizontal resolution for large scale structures is 0.5° of latitude or about 55 km at an altitude of 300 km. This would require 15 horizontal bins, resulting in 45 dimensions in the minimization of (15).

In this work, minimization is performed using the variable metric method of Broyden–Fletcher–Goldfarb–Shanno, a variation of the Davidon–Fletcher–Powell (DFP) method [25], [26]. This algorithm was selected due to its fast convergence and robust performance on nonlinear problems. The DFP algorithm makes explicit use of gradient information. The Jacobian gradient matrix for E has three rows given by

$$\nabla \mathbf{E} = \begin{pmatrix} \dfrac{dE}{d\mathbf{V}^m} \\ \dfrac{dE}{d\mathbf{Z}^m} \\ \dfrac{dE}{d\mathbf{H}} \end{pmatrix} \tag{23}$$

$\nabla \mathbf{E}$ can be calculated explicitly from (13)–(22).

IV. Gridding

To accelerate convergence for a wide range of initial guesses, a multi-resolution approach is implemented in the gridding. The initial latitude gridding is set to be larger than the largest structure expected in the reconstruction. The altitude gridding is flexible, but should be smaller than the smallest expected structure size in the features under study. After each minimization of E, the grid is redefined with twice the resolution, the previous rebinned solution being used as the new initial guess. Fig. 4 illustrates a sequence of grids. The refinement proceeds from two latitude grids in the first panel to ten in the last. The fields of view of a four-instrument system are also shown in Fig. 4 for reference.

Where the columns of $\mathbf{L}$ are very sparse (i.e., toward the edge of the overall field of view), large latitudinal bins are be placed and unaltered. Such bins serve to reconcile the total photon inventory in a region that is not well supported by the data. This is especially important for GAET of sources that extend outside the fields of view of the instruments (as will be demonstrated). This type of gridding also helps mitigate the problem of tropospheric scattering. It is the low elevation angles where tropospheric scattering adds the greatest uncertainty to the data. The solution in this region has low confidence, but will still be consistent with the data.

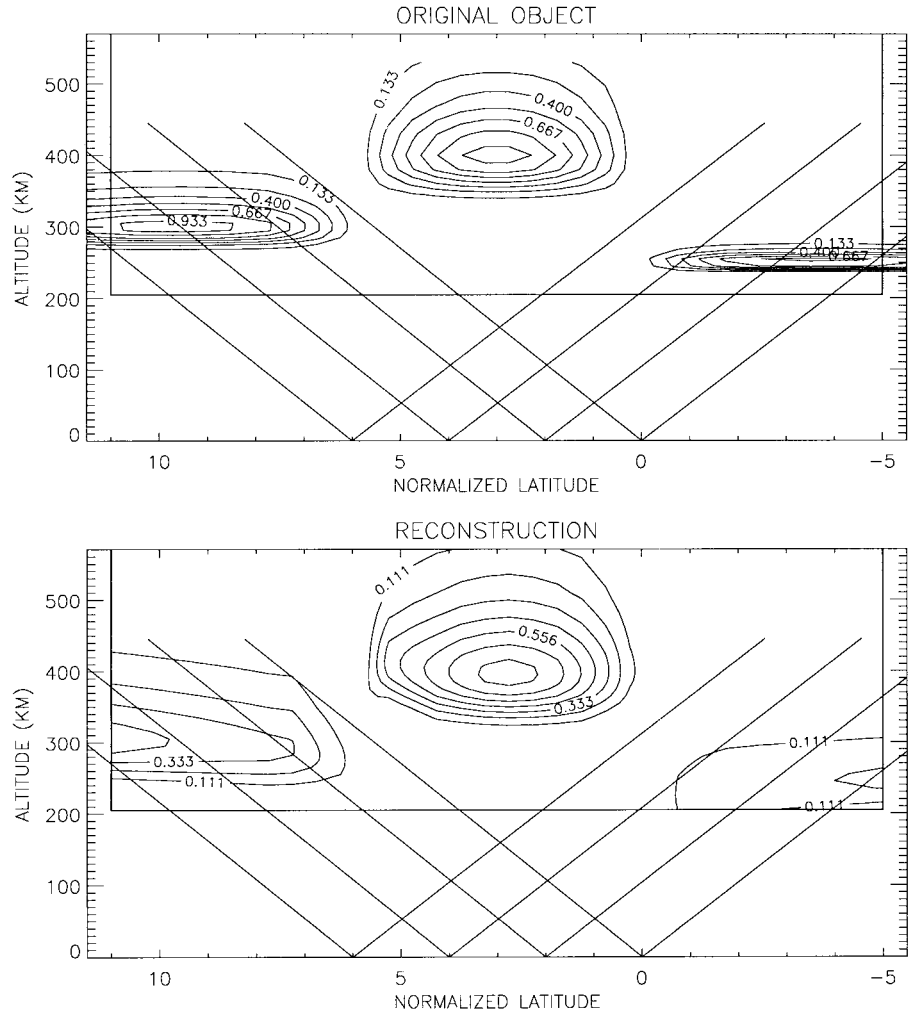

Fig. 7. The original object (upper panel) shows a central object and two objects that extend outside the field of view. This is a typical scenario for GAET. The central object is reconstructed well, while the outer extended emission layers are not well supported by the data. Highest confidence is placed in the region where the most observations overlap.

At some horizontal resolution, the data no longer supports the dimensionality of the solution, and the algorithm becomes unstable. The minimum horizontal resolution depends on the instrument separation and the type of structure in the emitting region. Although an absolute bound on the resolution cannot be determined explicitly, the multiresolution gridding provides a systematic way of determining the achievable resolution experimentally for a given problem. As the gridding is refined, the point at which the data no longer supports the desired horizontal resolution becomes obvious, as large numerical instabilities occur. For example, in tomography from four stations covering 6° of latitude, with a structured emission at 300 km altitude, the minimum resolution supported is about 0.25°, or 30 km.

After the best Chapman parameterization is found on the finest desired gridding, the Chapman constraint is removed. At this point, $\mathbf{v}$ is iterated on directly using MART (Multiplicative Algebraic Reconstruction Technique). MART minimizes the weighted residual two-norm with entropy regularization [27], [28]. MART can be thought of as minimizing (9) with $\mathbf{\Lambda} \cdot (\mathbf{v} - \mathbf{v}^*) = \mathbf{v} \ln \mathbf{v}$. MART converges to a positive solution with the greatest multiplicity amongst all feasible solutions within a neighborhood. As the full problem defined here is not strictly convex, MART will converge to a local minimum near the Chapman solution. An appropriate stopping criteria is $E \sim 1$. This indicates that the average residual is near the expected instrumental uncertainty.

V. Summary of Algorithm

The overall algorithm is described as follows.

1) Define initial reconstruction grid (I latitudes $\times$ J altitudes).
2) Calculate $\mathbf{L}$ from the observation and reconstruction geometries.
3) Minimize (22) using DFP method.
4) Adjust gridding to next finer resolution and repeat 2 and 3 with the current $\mathbf{V}^m$, $\mathbf{Z}^m$, and $\mathbf{H}$ as the initial guess.
5) When finest desired gridding is achieved, remove Chapman constraint and apply MART to the direct inverse problem using present value of $\mathbf{v}^c$ as the initial guess.

This algorithm incorporates many desirable features in regularizing the ill-posed GAET problem. First, it incorporates a minimum amount of *a priori* information. The vertical profile

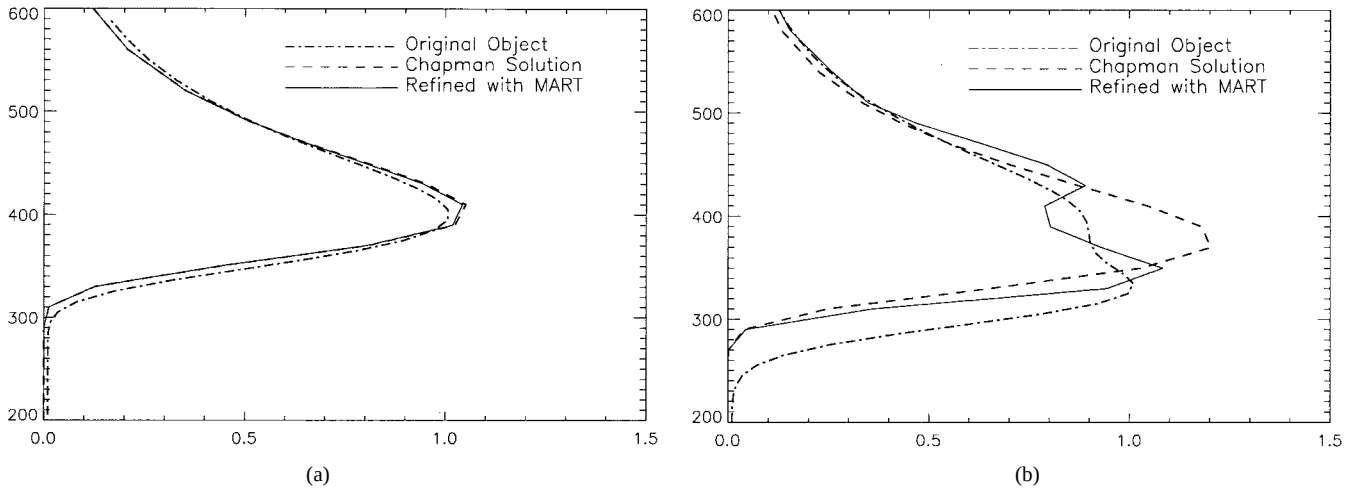

Fig. 8. (a) Vertical profile through the center of the Chapman phantom of Fig. 7, along with the reconstruction. The MART refinement adds no information to the solution in this case and (b) the original phantom in the center of Fig. 7 is replaced with the non-Chapman profile shown (dashed-dotted line). The Chapman solution overestimates the peak emission and peak altitude. The MART-refined solution results in a better fit, including approximating the phantom's bimodal structure.

of an emission layer has mean features which are well described by the parameterizing Chapman function. Second, the Chapman function along with constraints leads to an objective that has an explicit form for the gradient, allowing the use of minimization techniques that converge geometrically. Third, the multiresolution gridding scheme facilitates convergence for a wide variety of initial guesses, and provides a convenient means for finding the optimum spatial resolution supported by the data. Fourth, instrumental and atmospheric related uncertainties are handled automatically in the tomographic reconstruction. And lastly, refinement of the solution with MART allows fitting the data to any desired uncertainty.

VI. Simulations

In GAET, the detail to which an object may be reconstructed is limited primarily by the constrained viewing geometry. Even in the case of ideal noiseless data, and using the regularization scheme described above, artifacts and numerical instabilities can appear in the reconstruction if too fine a resolution is sought. Whether the reconstruction scheme used is constrained spectrally, unconstrained, model based, etc., care must be taken in choosing the solution dimension. The Chapman parameterization provides an intuitive means for evaluating such geometrical limitations. This is shown in the first example to follow. The subsequent three examples demonstrate the algorithm for typical but difficult atmospheric emission structures.

The simplest structure to consider in GAET, in terms of reconstruction, is a uniform stratified emitting region extending from horizon to horizon. If this layer is described by a Chapman function, then the inverse problem requires solving for only three parameters. This may not represent the most tractable problem, in the sense that horizontal structure helps define the vertical structure in the GAET geometry. But it does allow us to analyze the objective function (15) graphically, and therefore provides some insight into it's convexity.

The vertical profile of such a layer with $V^m = 1$, $Z^m = 300$ km, and $H = 30$ km is shown in the solid line of Fig. 3. In this ideal case, a single instrument provides the maximum information on the object (i.e., the measurements are independent of γ_P). Looking at equations (13)–(15), E is a linear function of V^m and thus $d^2E/dV^{m2} = 0$. Therefore, if E is convex with respect to Z^m and H, then it will also be convex with respect to V^m. Fig. 5 shows contours of E for a range of possible Z^m and H in the uniform stratified problem outlined above (in this case $Z_l^m = 100$, $Z_h^m = 500$, $H_l = 10$, and $H_h = 100$). In order for a steepest descent or quasi-Newton algorithm to converge to the global minimum, the initial guess must be in the region to the right of the partitioning line drawn. An initial guess to the left will converge to a solution in the valley.

Fig. 6 shows the values of E in the central valley of Fig. 5 as a function of both H and Z^m. Clearly E is not strictly convex. The unwanted local minimum has a large characteristic width and the lowest available altitude: essentially a uniform distribution of emission. We see that even in this simple problem, the forward transform from $\mathbf{v}$ to $\mathbf{d}$ is only uniquely reversible with a proper initial guess. This is purely a result of the limited angle nature of the observations, as the simulated data is noise free and the object is described exactly by a combination of the three parameters the algorithm seeks. In the full 50–100 dimensional problem, the effect of the initial guess on convergence cannot be determined explicitly. We must exercise the algorithm for a wide variety of typical emission structures to determine the robustness of the technique.

The feasibility region defined by Z_l^m, Z_l^h, H_l, and H_h of (17) reflect well known limits on the altitude and scale size of airglow and auroral structures. When implemented as barrier functions, they allow for larger step sizes in line searches during DFP minimization, yielding faster convergence. They also insure that the algorithm is exited gracefully when a local minimum (e.g., the valley of Fig. 5) is being pursued. If the solution is on the constraint boundary, the algorithm must be restarted with a different initial guess.

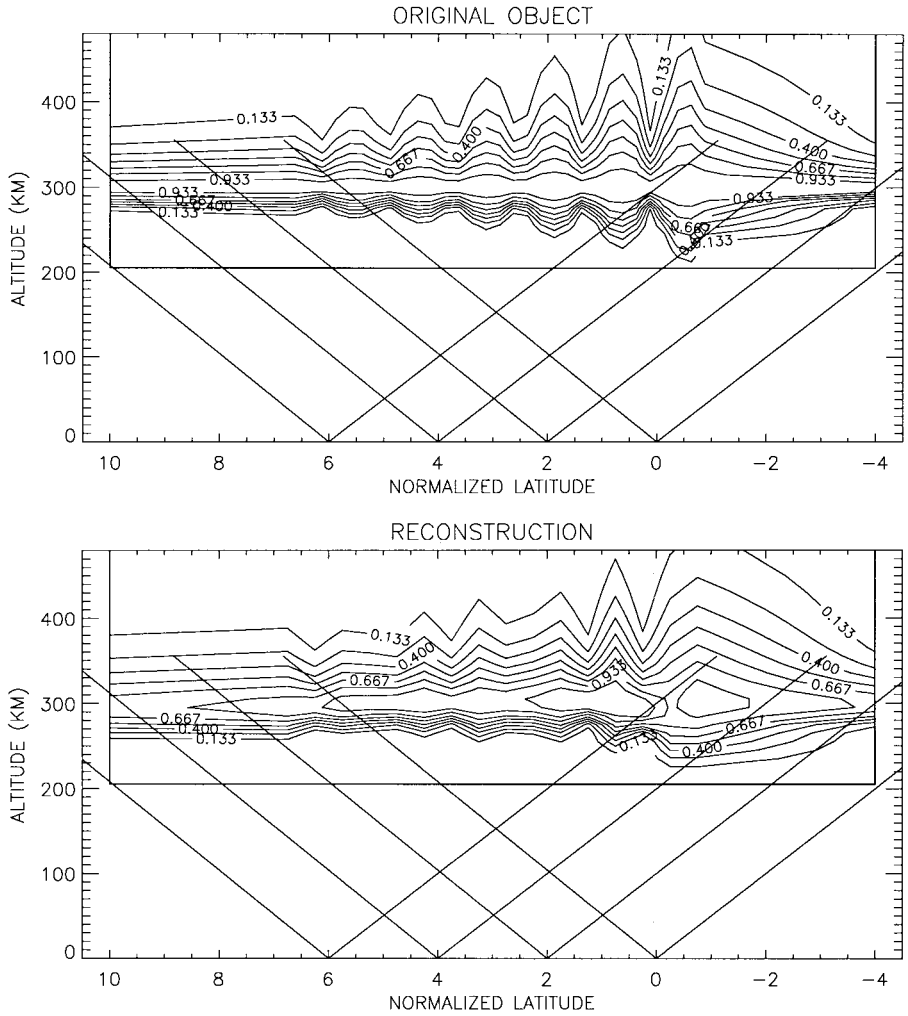

Fig. 9. The original object is a source extending from horizon to horizon. The structure has a variable characteristic width H. The reconstruction captures each of the maxima in H although the detail is somewhat smoothed.

We now present simulations of three different sample GAET reconstructions. In Figs. 7, 9, and 10, the original (phantom) object is in the upper panel, and the GAET reconstruction is in the lower panel. The fields of view from each of the four observing sites are shown. The sites are each separated by 2° on an Earth-centered polar coordinate system (i.e., Normalized Latitude $= \gamma_P$ of Figs. 2), or 223 km ground distance. Each projection has 140 evenly distributed samples (i.e., resolution elements in the measuring device). The phantom objects used in these examples highlight "difficult" objects typical of atmospheric emission structures. All reconstructions are obtained from the uniform stratified initial guess of $V^m = 1$, $Z^m = 350$, $H = 20$.

In GAET of discrete auroral arcs, an important issue is the contribution of distant emission sources to the observed data (such sources include background airglow and distant auroral arcs). These sources extend past the fields of view of all instruments and in fact may be completely outside the fields of view of at least one of the instruments. The top panel of Fig. 7 shows an isolated feature in the presence of two extended emitting layers (similar to a stable auroral red arc [29] within the mid-latitude ionospheric trough). The phantom structures in this case are Chapman functions in altitude.

The GAET algorithm is able to reconstruct the isolated feature amidst the two distant sources. The emitting layers at the outer edges are not well supported in the data and, hence, are not accurately reconstructed. The highest confidence in GAET reconstruction lies where the most lines of site overlap. To quantify the goodness of the reconstruction, Fig. 8(a) plots the profile through the center of the arc. Three vertical profiles are shown: the original phantom, the Chapman reconstruction, and the subsequent MART refinement (as labeled). As expected for this phantom, the MART refinement adds no additional information to the solution.

In order to test the robustness of the algorithm to a non-Chapman emitting layer, we created another auroral phantom by superposing a Gaussian and a Chapman emission profile centered at different altitudes. This structure was put in place of the central object of Fig. 7, with the outer structures the same. A vertical profile through this phantom is shown in the dashed line of Fig. 8(b) (as labeled). Both the Chapman result (dashed line) and the unconstrained MART reconstructed

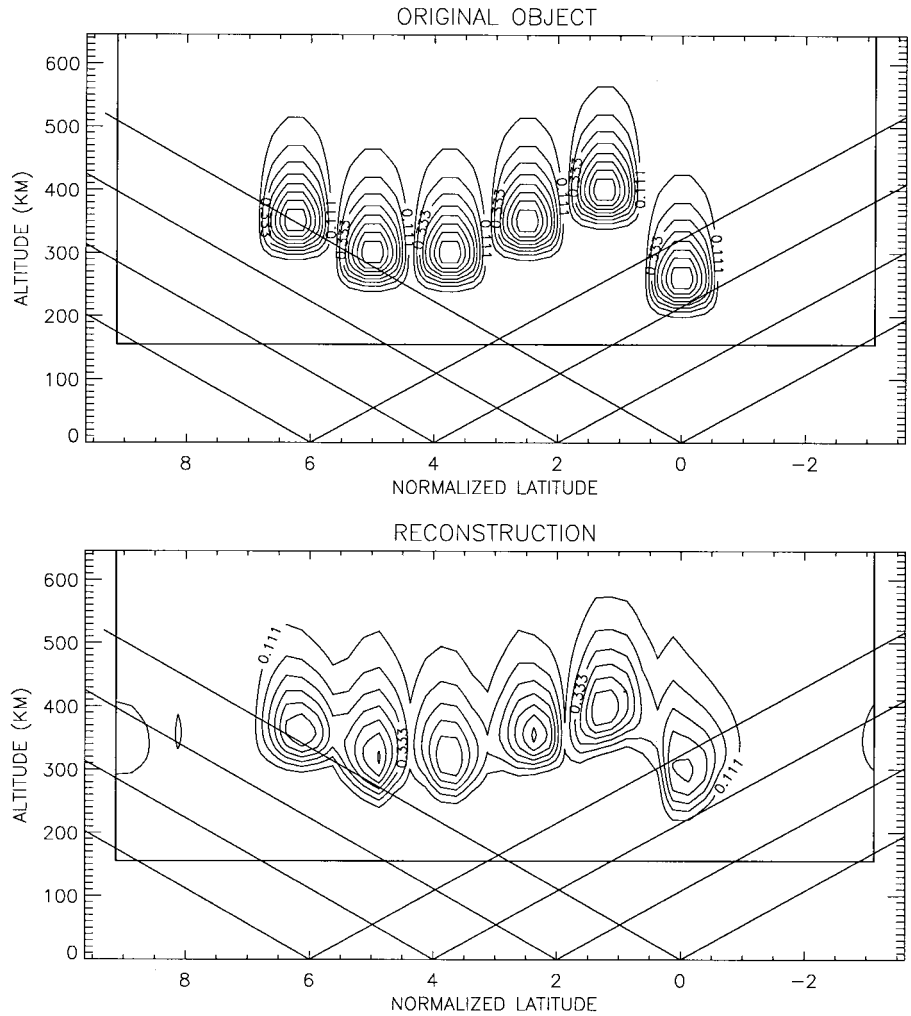

Fig. 10. The original objects are six identical Chapman structures with varying peak altitudes V^m. The reconstructed objects clearly show the altitude variation, although the peak emission is underestimated by about 20%.

(dashed-dotted line) profiles are also shown. Notice that the Chapman solution overestimates the peak emission rate and the peak altitude in an effort to match a very non-Chapman-like profile. The subsequent MART-refined solution captures well the peak emission rate and estimates the peak emission height to within 20 km. The bimodal nature of the phantom is also approximated in the MART-refined solution. The fit to the topside and bottomside remains relatively unchanged from the Chapman solution. The shapes of these two regions are again not well supported in the GAET data. Because MART favors a small solution norm, the larger volume emission rate elements are preferentially adjusted.

Fig. 9 shows an example of GAET of a continuous structured extended source. This case is typical of mid- and low-latitude emission, and represents one of the most difficult objects for GAET. In Fig. 9, the added structure is in the form of a variable emission layer *width* H. The GAET algorithm is able to locate each of the maxima. The detail is somewhat smoothed out. But it is encouraging to note that resolving the general morphology of an extended structured layer is a tractable problem.

Fig. 10 highlights another major problem for GAET: reconstruction of closely spaced arcs at varying altitudes. The phantoms are created using Chapman vertical profiles and sinusoidal horizontal profiles. *Fougere* [30] and others have noted that the inversion of such a structure would benefit from some observations from a horizontal direction (e.g., from a satellite-borne photometer). However, the peak emission altitude *is* supported by the data, although weakly so. The GAET algorithm presented here provides a reasonable reconstruction of the morphology of the original phantom, while underestimating the peak emission by $\sim$20%. Again, the solution converges from a uniform initial guess in each Chapman parameter and is not dependent on a detailed model of the emission layer.

The simulations presented here are a representative set of a large group of phantoms presented to this algorithm. The degree of detail that can be reconstructed in these objects is dependent on the type of structure present in the phantoms. We have shown that if we acknowledge the geometrical limitations on the solution to the GAET problem, we may reach a compromise between resolution and solution confidence. Nonlinear

optimization applied to GAET will provide hitherto untapped information about the physics of atmospheric emissions.

VII. Field Test

A network of imaging systems has been constructed and deployed to gather data for GAET. The system, called COTIF (CEDAR Optical Tomographic Imaging Facility) consists of three all-sky imaging spectrographs and an all-sky imaging system [19] placed in a line extending from Caribou, ME, to Block Island, RI, (about 500 km total separation). Initial results from COTIF have been presented in [31]. Coordinated radar and optical tomographic observations are currently being made as test cases for the GAET algorithms. Supporting data from the Millstone Hill Incoherent Scatter Radar will be used to model directly those features related to plasma processes.

VIII. Conclusions

We have considered the problem of determining the 2-D structure of optically thin atmospheric emissions using a set of 1-D observations. The linear system defined when the emitting region is discretized *a priori* is poorly conditioned. This is a direct result of the constrained observing geometry.

The ill-conditioning is mitigated through a natural parameterization in the vertical direction. At any given horizontal position, the vertical emission profile is constrained by three parameters: the maximum emission rate, the altitude of the maximum emission rate, and the characteristic width of the emitting region. We have shown that in the simple case of a uniform stratified emitting region, the resulting weighted-least-squares objective function is not strictly convex in the three parameters sought. The unwanted local minima are easily recognizable, but in the full $I \times J$ dimensional problem, the effect of the initial guess on the solution must be tested through simulation.

The combination of barrier functions and the explicit Chapman functional description lead to an unconstrained nonlinear optimization problem. Minimization is performed using the algorithm of Broyden–Fletcher–Goldfarb–Shanno, a variation of the Davidon–Fletcher–Powell (DFP). To accelerate convergence, and to provide a systematic means of evaluating the resolution, a multi-resolution gridding scheme is used. The problem is solved on successively finer horizontal grids. Deviations from a Chapman-like solution are allowed in the final step of the algorithm. The explicit functional description is removed, and the direct inverse problem is solved using the MART algorithm with the parameterized Chapman solution used as the initial guess.

This algorithm has been shown to reconstruct a variety of phantom objects that illustrate characteristic emission structures. In previous work on ionospheric radio-beacon tomography, the initial guess is often chosen from a set of model ionospheres. The solution is often constrained to be a linear combination of basis ionospheres. In these techniques, features of the initial guess (specifically, the layer width and peak altitude) often appear in the solution. The present nonlinear GAET algorithm reconstructs difficult features from a uniform stratified initial guess by pursuing a trade-off between resolution and accuracy.

An observing system has been constructed to implement the GAET technique, named COTIF for CEDAR Optical Tomographic Imaging Facility. COTIF consists of a chain of four portable imaging stations along the New England coast. These instruments are presently making coordinated observations with the Millstone Hill incoherent scatter radar.

Acknowledgment

The authors are grateful for the scientific and technical guidance provided by J. Baumgardner. The authors would also like to acknowledge G. Sandri, W. C. Karl, and D. Castanon for their help in reviewing and commenting on this work.

References

[1] J. W. Chamberlain, *Physics of Airglow and Aurora.* New York: Academic, 1961.
[2] M. Mendillo and J. Baumgardner, "Ground-based imaging of detailed arcs, ripples in the diffuse aurora, and patches of 6300 E emission," *J. Geophys. Res.*, vol. 94, no. A5, pp. 5367–5381, May 1989.
[3] S. C. Solomon, "Optical aeronomy," *U.S. Nat. Rep. Int. Union of Geod. Geophys. 1987–1990, Rev. Geophys.*, vol. 29, pp. 1089–1109, 1991.
[4] J. Semeter, M. Mendillo, J. Baumgardner, J. Holt, and V. Eccles, "A study of 6300Å airglow production through chemical modification of the nighttime ionosphere," *J. Geophys. Res.*, vol. 101, no. A9, pp. 19 683–19 699, Sept. 1996.
[5] M. Mendillo and J. Forbes, "Artificially created holes in the ionosphere," *J. Geophys. Res.*, vol. 83, no. A1, pp. 151–162, Jan. 1976.
[6] P. A. Bernhardt, "A critical comparison of ionospheric depletion chemicals," *J. Geophys. Res.*, vol. 92, no. A5, pp. 4617–4628, 1987.
[7] M. R. Bowman, A. J. Gibson, and M. C. W. Sandford, "Atmospheric sodium measured by a tuned laser radar," *Nature*, vol. 221, pp. 456–457, 1969.
[8] C. S. Gardner, "Sodium resonance fluorescence LIDAR applications in atmospheric science and astronomy," *Proc. IEEE*, vol. 77, p. 408, 1989.
[9] C. Tepley, I. Stoyan, and R. Rojas, "The Doppler Rayleigh LIDAR system at Arecibo," *IEEE Trans. Geosci. Remote Sensing*, vol. 31, p. 36, Jan. 1993.
[10] S. C. Solomon, P. B. Hays, and V. J. Abreu, "Tomographic inversion of satellite photometry," *Appl. Opt.*, vol. 23, p. 3409, 1984.
[11] ———, "Tomographic inversion of satellite photometry, Part 2," *Appl. Opt.*, vol. 24, p. 4134, 1985.
[12] I. C. McDade, N. D. Lloyd, and E. J. Llewellyn, "A rocket tomography measurement of the N2+ 3914A emission in an auroral arc," *Planet. Space Sci.*, vol. 39, no. 6, pp. 895–906, June 1991.
[13] D. Cotton, "Ionospheric tomography using EUV," *EOS*, vol. 74, p. 489, Nov. 1994.
[14] J. R. Austen, S. J. Franke, and C. H. Liu, "Ionospheric imaging using computerized tomography," *Radio Sci.*, vol. 23, no. 3, pp. 299–307, May/June 1988.
[15] T. D. Raymund, J. R. Austen, S. J. Franke, C. H. Liu, J. A. Klobuchar, and J. Stalker, "Application of computerized tomography to the inversion of ionospheric structures," *Radio Sci.*, vol. 25, no. 5, pp. 771–789, Sept./Oct. 1990.
[16] P. A. Bernhardt, J. D. Huba, P. K. Chaturvedi, J. A. Fulford, P. A. Forsyth, D. N. Anderson, and S. T. Zalesak, "Analysis of rocket beacon transmissions for computerized reconstruction of ionospheric densities," *Radio Sci.*, vol. 28, no. 4, pp. 613–627, July/Aug. 1993.
[17] Y. Censor, "Finite series expansion reconstruction methods," *Proc. IEEE*, vol. 71, no. 3, pp. 409–419, Mar. 1983.
[18] H. Takahashi, B. R. Clemesha, P. P. Batista, Y. Sahai, M. A. Abdu, and P. Muralikrishna, "Equatorial F-region OI 6300Å and OI 5577Å emission profiles observed by rocket-borne airglow photometers," *Planet. Space Sci.*, vol. 38, no. 4, pp. 547–554, Apr. 1990.
[19] J. Baumgardner, B. Flynn, and M. Mendillo, "Monochromatic imaging instrumentation for applications in aeronomy of the Earth and planets," *Opt. Eng.*, vol. 32, no. 12, pp. 3028–3032, Dec. 1993.
[20] C. W. Allen, *Astrophysical Quantities.* London, U.K.: Athlone, 1973.
[21] M. H. Rees and R. G. Roble, "Excitation of O(^{1}D)atoms in aurorae and emission of the [OI] 6300-Å line," *Can. J. Phys.*, vol. 64, p. 1608, 1986.
[22] S. Chapman, *Proc. Phys. Soc.*, London, U.K., 1931, vol. 43, no. 26.

[23] P. R. Adby and M. A. H. Dempster, *Introduction to Optimization Methods.* New York: Halsted, 1974.
[24] D. J. Wilde and C. S. Beightler, *Foundations of Optimization.* Englewood Cliffs, NJ: Prentice-Hall, 1967.
[25] E. Polak, *Computational Methods in Optimization.* New York: Academic, 1971.
[26] W. H. Press, *Numerical Recipes in C: The Art of Scientific Computing.* New York: Cambridge Univ. Press, 1988.
[27] R. Gordon, R. Bender, and G. T. Herman, "Algebraic reconstruction techniques (ART) for three-dimensional electron microscopy and X-ray photography," *J. Theoret. Biol.*, vol. 29, pp. 471–481, 1970.
[28] Y. Censor, "Row-action methods for huge and sparse systems and their applications," in *SIAM Rev.*, Oct. 1981, vol. 23, no. 4.
[29] M. H. Rees and R. G. Roble, "Observations and theory of the formation of stable auroral red arcs," *Rev. Geophys.*, vol. 13, pp. 201–242, Feb. 1975.
[30] P. Fougere, "Ionospheric radio tomography using maximum entropy, 1. Theory and simulation studies," *Radio Sci.*, vol. 30, no. 2, pp. 429–444, Mar./Apr. 1995.
[31] J. Semeter, M. Mendillo, M. Buonsanto, and P. Erickson, "Coordinated radar and optical tomographic imaging of mid-latitude airglow structures," *Trans. AGU*, vol. 77, p. 192, Apr. 1996.

Joshua Semeter received the B.S. degree in electrical engineering from the University of Massachusetts, Amherst, in 1987, and the M.S. and Ph.D. degrees in electrical engineering from Boston University, Boston, MA, in 1992 and 1997 respectively.

From 1987 to 1990, he was a Control Systems Engineer for Pratt and Whitney Aircraft. He is currently a Research Associate at Boston University's Center for Space Physics where he continues to develop the technique of ground-based atmospheric emission tomography. In September 1997, he joined the Max Planck Institute, Garching, Germany, as a Staff Scientist. His research interests involve characterizing energetic processes in the upper atmosphere through remote sensing of optical and radio emissions, and developing statistical image processing techniques for geophysical applications.

Dr. Semeter received two outstanding paper awards from the American Geophysical Union as a graduate student at Boston University for his work on ionospheric sounding rocket experiments.

Michael Mendillo is a Professor of Astronomy and Electrical Engineering at Boston University, Boston, MA, and a member of the Center for Space Physics. He teaches at both the undergraduate and graduate levels, specializing in astronomy for nonscience majors, and graduate courses in space physics. He heads an active research group that studies natural and artificially induced disturbances in the Earth's ionosphere, as well as studies of the distant atmospheres of Jupiter and the Moon. His research is supported by several National Aeronautics and Space Administration (NASA), National Science Foundation (NSF), and Department of Defense programs.

Dr. Mendillo also serves on various advisory committees for NASA, NSF, and the National Academy of Sciences.